KRONOS FUSION ENERGY

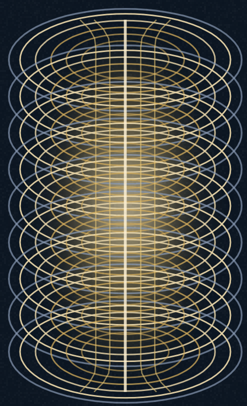

PAPER 2.20 · THE KRONOS 2026 SERIES

Poloidal-Field Coil Set and Equilibrium-Current Optimization for a Compact Spherical-Tokamak Breeder: Shaping the Negative-Triangularity, Solenoid-Free Equilibrium with Vertical-Stability Authority

The poloidal-field (PF) coils are what hold a strongly shaped, strongly elongated plasma in place: they must pull the outboard boundary inward to negative triangularity, sustain a...

Read it live — 3-D model · physics validator · film series

BY P I FORD, R J WEGGEL AND C WEGGEL

2026 · EDITORIAL EDITION

THE OFFICIAL RECORD

What this document is, and how to read its numbers

This is a combined editorial. It gathers, in one volume, the two design studies Kronos Fusion Energy released in 2026 — a compact spherical-tokamak tritium/helium-3 breeder and a deuterium–helium-3 tandem-mirror generator — together with the intellectual-property estate, the people, and, in the internal edition, the full commercial case. The scientific text is the same text that appears in the arXiv preprints and the journal submissions; the editorial adds the apparatus a reader needs to hold the whole program at once, and nothing in the physics is altered to fit it.

THE HONESTY STANCE IS THE ASSET

Every headline quantity carries an **evidence class** — DERIVED RECOMPUTED MEASURED REQUIREMENT — and, where a number is a modelled extrapolation rather than a demonstrated value, it is labelled as such and its downside is shown next to it. Several quantities in the underlying corpus moved after first publication; where a value has been withdrawn or restated, the record says so plainly. This is deliberate: a diligence team will find the load-bearing assumptions, so the document surfaces them first.

TWO EDITIONS

This volume is issued in two editions. The **public edition** (light) carries the physics and the design only — no dollar, price, or per-kilogram figure appears anywhere in it. The **internal edition** (dark) adds the economics, the funding architecture, and the defense-commercial analysis, and is marked *Confidential* accordingly; it is not for public distribution. Where the commercial case rests on a modelled assumption rather than a demonstrated one, it is labelled as such and its downside is shown alongside it, on the same terms as the physics.

TITLE	The Kronos Fleet — Hyperion · Aegis · MetroVolt: A Combined Design & Commercialization Study
AUTHOR	Priyanca Ford, Founder & CEO, on behalf of Kronos Fusion Energy
EDITION	2026 Combined Editorial · first issue
COMPANION WORKS	The five-paper arXiv drop — (1) Breeder, (2) Burner, (3) REBCO magnet & tape, (4) Direct Energy Conversion, (5) AI/ML/Quantum control — with matching numbered Zenodo deposits, plus the IOP journal and IAEA-FEC submissions. Patents were filed before the drop.
NAMING	Hyperion = the breeder; Aegis (defense) and MetroVolt (data-center) = one generator in two housings. Internal mode letters (D1, L) do not appear on public surfaces.
STATUS	Conceptual design & simulation study. Nothing herein is a construction commitment.

HOW TO READ THIS VOLUME

The fleet at a glance, and the way its numbers are marked

This volume opens with *Orientation*, presents the five research papers as a bound sequence, and closes with the *Apparatus*. *Foundations* sets out the three general results both machines rest on. *Paper One* is the Hyperion breeder; *Paper Two* the Aegis / MetroVolt generator; *Papers Three, Four and Five* are the enabling science — high-field REBCO magnets and tape, direct energy conversion, and the AI / ML / quantum control stack. A *Digital Twin & 3-D Model* part follows, then the *Environmental* profile. The *Economics* and levelized cost and the *Business Case* and diligence record appear in the internal edition only; the *Simulations* proof record and the Apparatus — patent portfolio, team, limitations, and sources — close both editions.

THE FLEET AT A GLANCE

	HYPERION	AEGIS	METROVOLT
Role	Strategic-isotope foundry	Defense installation power	Campus power
Machine	**Spherical tokamak**	**Tandem mirror**	**Tandem mirror**
Fuel	Deuterium–tritium	Deuterium–helium-3	Deuterium–helium-3
Delivers	Tritium · ^{3}He · 14 MeV n	Resilient installation power	Firm campus power
Physics bar	**Fusion gain only**	Closure (gates named)	Closure + lunar ^{3}He
In the fleet	Breeds the fuel	Proves the generator	Commercial destination

HOW THE NUMBERS ARE MARKED

Every headline quantity carries an evidence class — DERIVED from first principles, RECOMPUTED from raw data, MEASURED in hardware, or a REQUIREMENT yet to be met. Financial figures carry a case label and are confined to the internal (confidential) edition. Values that moved after first publication are shown as withdrawn or restated rather than quietly changed. A capability you can evaluate is one whose limits are on the page.

ABSTRACT

Poloidal-Field Coil Set and Equilibrium-Current Optimization for a Compact Spherical-Tokamak Breeder: Shaping the Negative-Triangularity, Solenoid-Free Equilibrium with Vertical-Stability Authority

The poloidal-field (PF) coils are what hold a strongly shaped, strongly elongated plasma in place: they must pull the outboard boundary inward to negative triangularity, sustain a doubling elongation against its own ideal vertical instability, and set the divertor null, while the toroidal-field magnet does its own, entirely separate job. We pose the coil-current problem for a compact negative-triangularity spherical-tokamak breeder (design point $I_p = 9.66$ MA, $Q = 3.076$, $P_{\mathrm{fus}} = 85.04$ MW, $\delta = -0.30$, $\kappa = 2.0$, $B_0 = 8$ T, $R_0 = 1.20$ m, aspect ratio $A = 2.5$) as a regularized inverse free-boundary problem: sixteen isoflux constraints on a Miller negative-triangularity boundary, a two-parameter current-profile family pinned to the poloidal beta and the plasma current, and the coil currents recovered by a Tikhonov least-squares over the vacuum Green's functions at each Picard step of a free-boundary Grad–Shafranov solve. We derive the governing equations, the inverse-problem formulation, and the numerical scheme — a five-point discretization of the elliptic operator on a 129×129 grid, a von Hagenow free-boundary treatment, and Picard iteration to a relative flux tolerance of 10^{-6} — and we report the converged equilibrium: $I_p = 9.660$ MA, $\beta_p = 0.3712$, separatrix $\delta = -0.334$ (the negative-triangularity shape holds), edge safety factor $q_{95} = 2.90$ (within $3.4\,\%$ of the 3.0 target), internal inductance $\ell_i(3) = 1.40$, on-axis pressure 1.21×10^7 Pa, and plasma volume 13.84 m ^{3}. A first-pass ideal-MHD screen places the equilibrium at a normalized beta $\beta_N = 2.13$, a factor 1.64 below the no-wall Troyon limit; a stricter reduced-metric n=1 kink screen makes the external kink the binding constraint at a margin of 1.15–1.31, with the Mercier and ballooning criteria satisfied on every confinement surface and violations confined to the $q < 1$ sawtoothing core. The PF set carries the equilibrium vertical field $B_v \approx 2.1$ T set by the Shafranov relation and delivers the vertical-position authority that a $\kappa = 2.0$ column demands. All results were produced by an NVIDIA GPU HPC campaign (FreeGS/FreeGSNKE free-boundary solves, DCON/GPEC stability screens, and a physics-informed equilibrium surrogate that reproduces the solver to $0.14\,\%$ RMS flux at a $2877\times$ inference speedup) and are frozen anchors in the Kronos de-risking register. The coil set is a distinct magnet system from the 16.84 T centrepost toroidal-field magnet and the 26.49 T burner plug coil.

Open-access deposit (code & data, CC BY 4.0): DOI 10.5281/zenodo.22645945 · Zenodo community *kronos_fusion_energy*. Explore it live: interactive 3-D model · physics validator.

Keywords: poloidal-field coils · equilibrium-current optimization · inverse isoflux · free-boundary equilibrium · negative triangularity · vertical stability · spherical-tokamak breeder

CONTENTS

Table of Contents

Poloidal-Field Coil Set and Equilibrium-Current Optimization for a Compact Spherical-Tokamak Breeder: Shaping the Negative-Triangularity, Solenoid-Free Equilibrium with Vertical-Stability Authority 3
Introduction 7
The coil set and the design point 8
Governing equations and the formal problem 10
Computational methodology: the NVIDIA GPU HPC campaign 13
Results 14
Discussion 24
Limitations 25
Conclusion 26
References 31
One programme, many papers 34

NOMENCLATURE

Symbols, units, and the names of things

Q	plasma (fusion) gain, P_{fus}/P_{aux}
Q_E	engineering gain, net electric out / recirculating in
H_{98}	confinement enhancement over the IPB98(y,2) scaling
Z_{eff}	effective ion charge
c_{ee}	electron–electron bremsstrahlung leading coefficient, 2.120022 (exact)
τ_E	energy confinement time
I_p	plasma current
R_0, a	major radius, minor radius
κ, δ	elongation, triangularity
β_N	normalized plasma beta (Troyon-normalized)
TBR	tritium breeding ratio
DEC	direct energy conversion
CF	plant capacity factor (availability)
FOAK / NOAK / BOAK	first / n^{th} / best of a kind
Hyperion	the ST breeder (internal: Mode D2)
Aegis	the generator, defense/installation housing (internal: Mode M)
MetroVolt	the generator, data-center housing (Mode M)

poloidal-field coils; equilibrium-current optimization; inverse isoflux; free-boundary equilibrium; negative triangularity; vertical stability; spherical-tokamak breeder

§ 1

Introduction

A negative-triangularity (NT) spherical tokamak asks a great deal of its poloidal-field (PF) coils. The coils must pull the outboard last-closed flux surface inward to hold a triangularity $\delta = -0.30$; they must impose and then hold an elongation $\kappa = 2.0$ that is ideally unstable to vertical displacement and must be actively controlled; they must position the magnetic axis and set the divertor null; and they must do all of this at a small aspect ratio ($A = 2.5$), where the plasma sits close to the coils and the shaping authority is both stronger and more delicate. Meanwhile the toroidal-field (TF) magnet — a demountable, radiation-consumable centrepost running at a 16.84 T peak field — does an entirely separate job, and the two magnet systems must be kept distinct in the analysis, not conflated.

This paper presents the breeder's PF coil set, the equilibrium-current optimization that produces the target boundary, and the free-boundary Grad–Shafranov solution that verifies the currents hold the design point with an ideal-MHD stability margin. The result underwrites the magnetic geometry of the Hyperion breeder: the design point $Q = 3.076$, $P_{\text{fus}} = 85.04$ MW, $I_p = 9.66$ MA at $B_0 = 8$ T is only meaningful if the negative-triangularity, high-elongation boundary that carries it is a physically realizable free-boundary equilibrium at the frozen current, field, and pressure. We show that it is.

WHY THE SHAPE, AND WHY IT IS HARD

Negative triangularity is not a cosmetic choice. At the Hyperion operating point it suppresses ion- and electron-scale turbulence and admits an ELM-free edge, and the companion nonlinear-gyrokinetic result establishes the transport quiescence that motivates the shape [35]. But the same shape that quiets the turbulence sharpens the coil problem: an NT boundary requires the outer shaping coils to *pull* the boundary against its natural tendency to bulge outward, and it does so at high elongation, where the vertical instability grows on the ideal Alfv\'enic timescale unless a conducting structure and a fast radial-field actuator hold it. The PF set is therefore simultaneously a shaping system and a stabilization system, and the two functions are coupled through the same currents.

PRIOR ART

The free-boundary equilibrium problem for axisymmetric toroidal plasmas is classical. Grad and Rubin [1] and Shafranov [2] established the force-balance equation that bears their names; Lackner [3] and von Hagenow gave the practical free-boundary computation that couples the plasma to external coils through vacuum Green's functions; Luxon and Brown [4] and Lao *et al.* [5] turned the forward problem into the equilibrium-reconstruction machinery (EFIT) that underlies tokamak operation today. The inverse problem — given a desired boundary, find the coil currents — is the design-time counterpart of reconstruction and is solved routinely by isoflux or flux-matching least-squares over the coil set [7]. Modern open-source solvers such as FreeGS [8] and its evolutive successor FreeGSNKE [9] implement the free-boundary solve with Newton–Krylov acceleration and expose the constrained-profile families we use here.

The stability side is equally well developed. The Mercier criterion [10] governs local interchange stability; the ballooning theory of Connor, Hastie and Taylor [11] governs high-n pressure-driven modes; the Troyon scaling [12] sets the normalized-beta limit for the global external kink; and the direct-criterion machinery of Newcomb, implemented in DCON [15] and extended to three-dimensional perturbed equilibria in GPEC/IPEC [16], provides the n=1 ideal eigenvalue. Vertical stability at high elongation has its own literature — the rigid-displacement and stability-margin models of Lazarus *et al.* [17], Portone [18], and Humphreys *et al.* [19] — and the negative-triangularity confinement advantage that motivates our shape has been demonstrated experimentally on TCV and DIII-D [21,22,23] and, in comparison with positive triangularity, since Lazarus *et al.* [20]. The spherical-tokamak configuration itself traces to Peng and Strickler [24] and has matured into compact-pilot and fusion-nuclear-science-facility concepts [25,26].

CONTRIBUTION

Against this background our contribution is fourfold. (i) We pose the breeder coil-current problem as a *regularized inverse free-boundary problem* and give it explicitly: the isoflux constraints, the Green's-function response, the Tikhonov least-squares recovered at each Picard step, and the two-parameter current-profile family pinned to β_p and I_p. (ii) We solve it to a converged free-boundary equilibrium that holds the negative-triangularity design point and report the full scalar set against target. (iii) We screen the equilibrium for ideal-MHD stability — Mercier, ballooning, and the Troyon/kink limit — and identify the binding constraint. (iv) We quantify the vertical-stability authority the PF set must deliver at $\kappa = 2.0$ and keep the PF system rigorously separate from the TF and plug magnets. Throughout, the numbers are frozen anchors of the Kronos de-risking register (serials BR-L1-A12 and BR-L2-A19) [32], and the whole solve was produced by an NVIDIA GPU HPC campaign that we document in Section 4. The coil solution feeds directly into the solenoid-free current-sustainment and startup design [36,37], the vertical-stability and VDE-avoidance study [34], the real-time control suite [38], and the companion free-boundary equilibrium and ideal-MHD paper [33].

§ 2

The coil set and the design point

The breeder carries an eight-coil PF set plus a central solenoid (Table 1, Figure 1): three up–down shaping pairs (P1–P3) that set the elongation and the negative triangularity, a single outboard coil (P4) that pulls the boundary and anchors the null, and a twenty-turn central solenoid (CS) for flux. The set rings a compact plasma at major radius $R_0 = 1.20$ m and minor radius $a = 0.48$ m; the shaping pairs sit close to the plasma so that they retain shaping authority at the small aspect ratio $A = 2.5$.

COIL	R (M)	Z (M)	ROLE
P1U / P1L	0.55	± 1.50	inner shaping / elongation
P2U / P2L	1.60	± 1.40	mid shaping
P3U / P3L	2.30	± 0.80	outer shaping / triangularity
P4	2.50	0.00	outboard / null anchor
CS	0.25	$-1.6 \ldots +1.6$	central solenoid (20 turns)

The eight-coil PF set and central solenoid (positions in metres), from the exact free-boundary machine definition (register serial BR-L1-A12). Up–down pairs are wired in mirror circuits carrying equal current for up–down symmetry; the outboard coil P4 anchors the null.

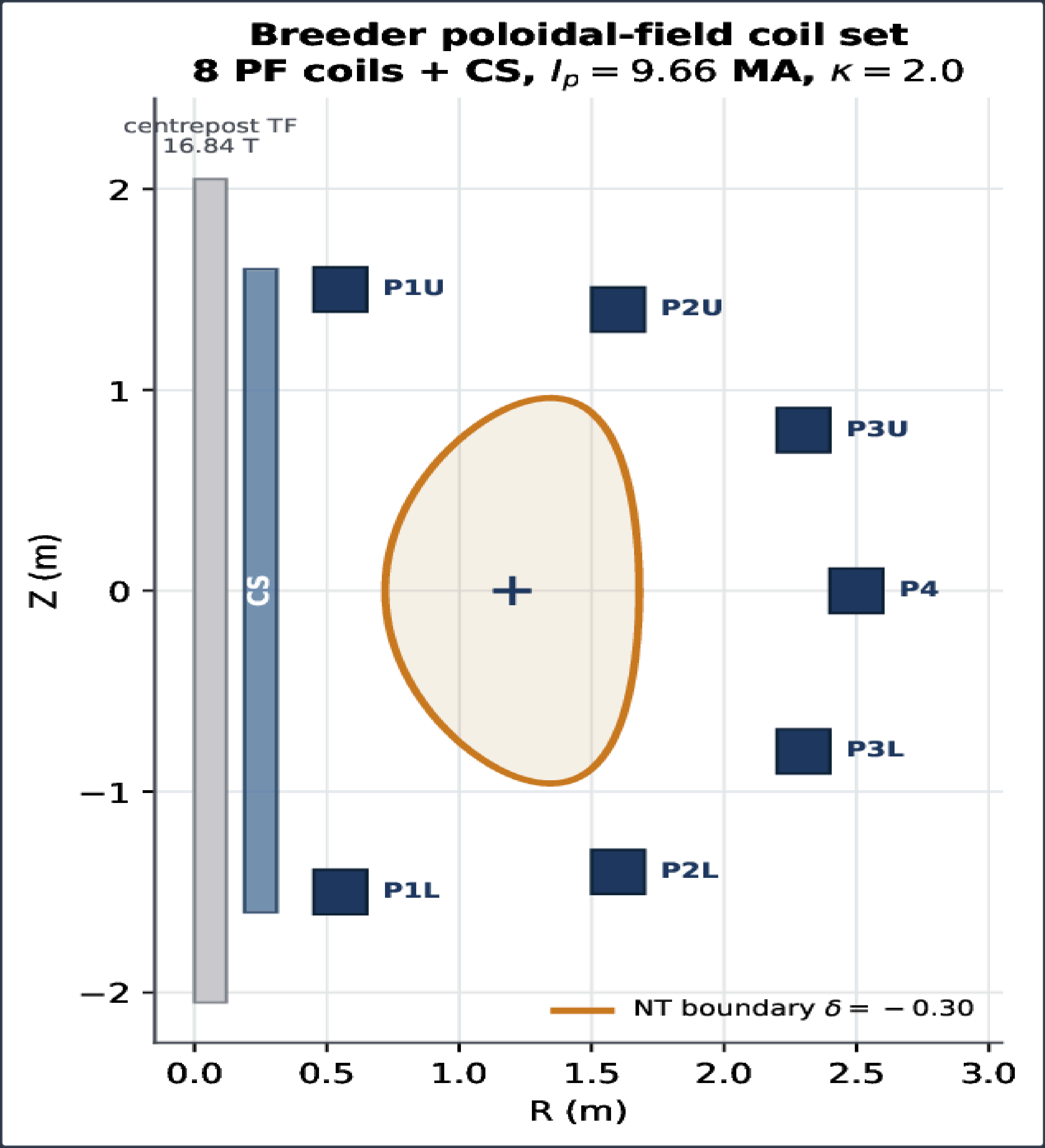

The breeder poloidal-field coil set holding the negative-triangularity boundary ($\delta = -0.30$, $\kappa = 2.0$) at $I_p = 9.66$ MA. Eight PF coils (P1–P4) and the central solenoid (CS) are shown with the plasma boundary and magnetic axis. The centrepost toroidal-field magnet (16.84 T peak) is drawn as the grey inboard leg and is a distinct device, not a PF coil. (Schematic; coil positions are the exact machine definition of Table 1.)

The vacuum toroidal field is set by the flux function $F(\psi) = R\,B_\phi$, which for the design point takes the edge value $F_{\text{vac}} = R\,B_\phi = 9.6$ T m, so that $B_\phi(R_0) = 9.6/1.20 = 8.0$ T on axis and rises to $9.6/(R_0 - a) = 13.3$ T at the inboard plasma edge; the centrepost conductor itself peaks at 16.84 T. That toroidal system is a distinct magnet, analysed separately from the equilibrium; here it enters only as the fixed F that the Grad–Shafranov operator requires.

§ 3

Governing equations and the formal problem

FREE-BOUNDARY GRAD–SHAFRANOV EQUILIBRIUM

Axisymmetric ideal-MHD force balance, $\nabla p = \mathbf{j} \times \mathbf{B}$, reduces to the Grad–Shafranov equation for the poloidal flux $\psi(R, z)$,

$$\Delta^* \psi \;=\; -\,\mu_0 R^2 \frac{dp}{d\psi} \;-\; F \frac{dF}{d\psi}, \qquad \Delta^* \;\equiv\; R \frac{\partial}{\partial R}\left(\frac{1}{R} \frac{\partial}{\partial R} \right) + \frac{\partial^2}{\partial z^2},$$

where $p(\psi)$ is the plasma pressure, $F(\psi) = R\,B_\phi$ the toroidal flux function, and μ_0 the permeability of free space. The toroidal current density is

$$j_\phi(R, \psi) \;=\; R \frac{dp}{d\psi} \;+\; \frac{1}{\mu_0 R}\, F \frac{dF}{d\psi},$$

and the plasma current is $I_p = \int_{\Omega_p} j_\phi \, dR\, dz$ over the plasma cross-section Ω_p, the region enclosed by the last-closed flux surface (LCFS). The free-boundary problem couples Equation 1 inside Ω_p to the vacuum field produced by the external coils: outside the plasma the current density is that of the coils, $j_\phi^{\mathrm{ext}} = \sum_c (I_c/A_c)\, \mathbf{1}_{\Omega_c}$, so that on the whole computational domain

$$\Delta^* \psi \;=\; -\mu_0 R \left[\, j_\phi^{\mathrm{pl}}(R, \psi)\, \mathbf{1}_{\Omega_p} \;+\; \textstyle\sum_c (I_c/A_c)\, \mathbf{1}_{\Omega_c} \right],$$

with I_c the current in coil c (cross-sectional area A_c). The plasma region Ω_p is itself unknown and is defined implicitly by the flux: $\Omega_p = \{(R, z) : \psi(R, z) \geq \psi_{\mathrm{b}}\}$, where the boundary flux ψ_{b} is the larger of the value at the limiter contact and the value at the active X-point. This implicit dependence of Ω_p on ψ is what makes the problem nonlinear and free-boundary.

THE VACUUM RESPONSE AND GREEN'S FUNCTIONS

The flux from the coils is linear in the coil currents. For a filamentary loop at (R', z') the axisymmetric Green's function of Δ^* is

$$G(R, z; R', z') \;=\; \frac{\mu_0}{2\pi} \frac{\sqrt{RR'}}{k} \left[(2 - k^2) K(k) - 2E(k) \right], \qquad k^2 = \frac{4RR'}{(R + R')^2 + (z - z')^2},$$

with K, E the complete elliptic integrals of the first and second kind. The externally applied flux at any field point is then

$$\psi_{\mathrm{ext}}(R, z) \;=\; \sum_c I_c\, \mathcal{G}_c(R, z), \qquad \mathcal{G}_c(R, z) = \int_{\Omega_c} \frac{G(R, z; R', z')}{A_c}\, dR'\, dz',$$

so that the coil-to-point response $\mathcal{G}_c$ is a precomputable geometric quantity. The total flux is the sum of the plasma-induced flux and the external flux, $\psi = \psi_{\mathrm{pl}} + \psi_{\mathrm{ext}}$, where ψ_{pl} obeys $\Delta^* \psi_{\mathrm{pl}} = -\mu_0 R\, j_\phi^{\mathrm{pl}}$ with the free-space (homogeneous) boundary condition supplied by the von Hagenow method (Section 4).

THE MILLER NEGATIVE-TRIANGULARITY BOUNDARY

The target LCFS is a Miller-parametrized negative-triangularity contour [6],

$$R(\theta) = R_0 + a \cos\!\big(\theta + \arcsin\delta\, \sin\theta\big), \qquad z(\theta) = \kappa\, a\, \sin\theta,$$

with $(R_0, a, \kappa, \delta) = (1.20\ \mathrm{m},\ 0.48\ \mathrm{m},\ 2.0,\ -0.30)$. The sign of δ is the whole point: with $\delta < 0$ the boundary curvature is reversed on the outboard midplane, and the coil set must supply the field that holds that reversed curvature against the outward hoop force. We sample Equation 6 at $M = 16$ control points $\{(R_k, z_k)\}_{k=1}^{M}$, uniformly in θ, to define the isoflux constraints.

THE INVERSE ISOFLUX CURRENT PROBLEM

The coil currents are not prescribed — they are solved for. The requirement that all sixteen control points lie on the *same* flux surface is the isoflux condition

$$\psi(R_k, z_k) \;=\; \psi(R_{k+1}, z_{k+1}), \qquad k = 1, \ldots, M-1,$$

together with an X-point condition $\nabla\psi|_{\mathrm{X}} = 0$ at the desired null. Writing $\psi = \psi_{\mathrm{pl}} + \sum_c I_c \mathcal{G}_c$ and taking differences against a reference point k_0, the isoflux constraints become *linear* in the currents:

$$\sum_c I_c \left[\mathcal{G}_c(R_k, z_k) - \mathcal{G}_c(R_{k_0}, z_{k_0})\right] \;=\; \psi_{\mathrm{pl}}(R_{k_0}, z_{k_0}) - \psi_{\mathrm{pl}}(R_k, z_k) \;\equiv\; b_k,$$

so that with the response matrix $A_{kc} = \mathcal{G}_c(R_k, z_k) - \mathcal{G}_c(R_{k_0}, z_{k_0})$ the coil-current vector $\mathbf{I} = (I_1, \ldots, I_{N_c})^\top$ solves the overdetermined system $A\mathbf{I} = \mathbf{b}$ ($M-1$ equations, N_c coils). Because the shaping coils are geometrically close and the response matrix is ill-conditioned, we regularize with a Tikhonov penalty on the current magnitude,

$$\mathbf{I}^\star \;=\; \arg\min_{\mathbf{I}} \; \left\|A\mathbf{I} - \mathbf{b}\right\|_2^2 \;+\; \lambda^2 \left\|\Lambda\,\mathbf{I}\right\|_2^2, \qquad \mathbf{I}^\star = \left(A^\top A + \lambda^2 \Lambda^\top \Lambda\right)^{-1} A^\top \mathbf{b},$$

where Λ weights the coils (here diagonal, penalizing the far coils more) and λ is chosen on the L-curve knee so that the boundary error and the current norm are simultaneously small. Equation 9 is the design-time inverse of the reconstruction least-squares of EFIT [5]: reconstruction fits currents to measured flux, whereas here we fit currents to a *desired* flux surface.

PINNING THE PROFILES: THE CONSTRAINED CURRENT FAMILY

The right-hand side ψ_{pl} in Equation 8 depends on the free functions $p(\psi)$ and $F(\psi)$. We adopt the standard two-parameter current family

$$\frac{dp}{d\psi} = \beta_0\,\frac{R_0}{\mu_0}\left(1 - \psi_N^{\alpha_m}\right)^{\alpha_n}, \qquad F\frac{dF}{d\psi} = (1-\beta_0)\,\mu_0 R_0\left(1 - \psi_N^{\alpha_m}\right)^{\alpha_n},$$

with $\psi_N = (\psi - \psi_{\mathrm{axis}})/(\psi_{\mathrm{b}} - \psi_{\mathrm{axis}})$ the normalized flux and (α_m, α_n) shape parameters. The two scale factors — equivalently the pair (β_0, **overall current amplitude**) — are determined by two integral constraints imposed at every iterate:

$$I_p = \int_{\Omega_p} j_\phi\, dR\, dz \;=\; 9.66\ \mathrm{MA},$$

$$\beta_p = \frac{\langle p\rangle}{B_{p,a}^2/2\mu_0} = \frac{2\mu_0}{B_{p,a}^2}\,\frac{\int_{\Omega_p} p\, dR\, dz}{\int_{\Omega_p} dR\, dz} \;=\; 0.3712,$$

where $B_{p,a} = \mu_0 I_p / L_p$ is the poloidal field averaged over the boundary of length L_p. Constraint 11–11 is the `ConstrainBetapIp` family: it fixes the poloidal beta at the canonical zero-dimensional value $\beta_p = 0.37125$ and the plasma current at 9.66 MA, leaving the shaping to the isoflux solve. The coupled system — Equation 3 for ψ, Equation 9 for the currents, and Equations 11–11 for the profile scale — is the formal problem.

IDEAL-MHD STABILITY METRICS

The converged equilibrium is screened for ideal-MHD stability by three reduced metrics evaluated on the flux surfaces. Local interchange stability is governed by the Mercier criterion [10],

$$D_M \;=\; D_R + \left(H - \tfrac{1}{2}\right)^2 \;>\; 0, \qquad D_R \;=\; \frac{\mu_0}{|\nabla\psi|^2}\,\frac{dp}{d\psi}\,\left\langle \cdots \right\rangle \;+\; (\text{shear, well terms}),$$

where the bracketed flux-surface averages combine the magnetic-well, shear, and pressure-gradient contributions in the standard form; $D_M > 0$ is stability. High-n pressure-driven ballooning stability is assessed in the s–α representation [11], with the magnetic shear and normalized pressure gradient

$$s \;=\; \frac{r}{q}\,\frac{dq}{dr}, \qquad \alpha \;=\; -\frac{2\mu_0 R_0 q^2}{B_0^2}\,\frac{dp}{dr},$$

and the operating locus of each surface compared with the first-stability boundary. The global external kink is screened by the Troyon normalized-beta limit [12],

$$\beta_N \;=\; \frac{\beta_t\,[\%]\;a\,[\mathrm{m}]\;B_0\,[\mathrm{T}]}{I_p\,[\mathrm{MA}]} \;<\; g_{\mathrm{T}},$$

with $g_{\mathrm{T}}{\approx}3.5$ the no-wall coefficient in the toolkit screen and $g{\approx}2.8$ a stricter reduced-metric no-wall kink value; the eventual arbiter is the direct $n{=}1$ ideal δW eigenvalue of DCON [15], which we flag as owed in Section 7.

VERTICAL STABILITY AND THE SHAFRANOV VERTICAL FIELD

An up–down-symmetric elongated plasma is in force balance in the radial direction only if the PF set supplies a vertical field. Averaging the radial force balance over the plasma gives the Shafranov vertical field

$$B_v \;=\; \frac{\mu_0 I_p}{4\pi R_0}\left[\ln\frac{8R_0}{a} + \beta_p + \frac{\ell_i}{2} - \frac{3}{2}\right].$$

Inserting the converged scalars ($R_0 = 1.20$ m, $a = 0.48$ m, $I_p = 9.66$ MA, $\beta_p = 0.371$, $\ell_i = 1.40$) gives $\ln(8R_0/a) = \ln 20 = 3.00$ and a bracket $3.00 + 0.371 + 0.70 - 1.50 = 2.57$, so

$$B_v \;=\; \frac{\mu_0(9.66\times 10^6)}{4\pi(1.20)}\,(2.57) \;\approx\; 2.1\ \mathrm{T},$$

the net vertical field the PF set must produce. But the same elongation that requires B_v makes the equilibrium vertically *unstable*: a rigid vertical displacement ξ_z of the current channel in the applied field produces a destabilizing force whenever the field decay index

$$n \;=\; -\,\frac{R_0}{B_v}\,\frac{\partial B_z}{\partial R}\bigg|_{\mathrm{axis}}$$

is negative, which it is for an elongated, up–down-shaped plasma. The rigid-mode equation of motion, retaining the passive stabilizing currents induced in the surrounding conducting structure and the active radial field B_r^{act} from the control coils, is

$$m_p\,\ddot{\xi}_z \;=\; 2\pi R_0 I_p\Big[\,B_r^{\mathrm{ind}}(\xi_z,\dot{\xi}_z) + B_r^{\mathrm{act}}\Big] \;-\; k_s\,\xi_z, \qquad k_s = 2\pi R_0 I_p\,\frac{\partial B_r}{\partial z} < 0,$$

where $k_s < 0$ is the open-loop destabilizing stiffness. In the massless (resistive-wall) limit the induced currents decay on the wall L/R time τ_w, and the open-loop growth rate reduces to $\gamma\,\tau_w = (1-m_s)/m_s$ in terms of a stability margin $m_s \in (0,1]$ set by the wall proximity and the decay index; the closed-loop system is stabilized by an active radial field whose gain the PF/control set must deliver [17,18,19]. The internal inductance $\ell_i(3) = 1.40$ enters both Equation 15 and the required control gain, tying the current-profile peaking to the vertical-control budget.

§ 4

Computational methodology: the NVIDIA GPU HPC campaign

CODES AND CAMPAIGN

Every number in this paper was produced on the Kronos NVIDIA GPU HPC platform — an in-house estate of A100-80 GB and H100-class accelerators together with single A100/H100/A10 nodes for the offline multi-physics sweeps — with the reduced-order and analytic gates run on the in-house HPC node (56-thread, 768 GB). The free-boundary equilibrium is solved with FreeGS 0.8.2 [8] and cross-checked with its evolutive Newton–Krylov successor FreeGSNKE [9]; the ideal-MHD screens use the Mercier and ballooning reduced metrics validated against the classical s–α first-stability boundary, with the direct n=1 criterion staged on DCON/GPEC [15,16]. The equilibrium was rebuilt bit-identically across the two register serials that anchor it (BR-L1-A12 and BR-L2-A19), reproducing $I_p = 9.660$ MA, $\beta_p = 0.3712$, and $V = 13.84$ m^3 on both [32]. No cost or budget figures attach to any of this; the campaign is described purely by its codes, scale, and reproducibility.

DISCRETIZATION OF THE ELLIPTIC OPERATOR

The operator Δ^* is discretized on a uniform $N_R \times N_z = 129 \times 129$ grid by the standard five-point stencil that respects the $1/R$ weighting,

$$(\Delta^*\psi)_{i,j} \approx \frac{\psi_{i+1,j} - 2\psi_{i,j} + \psi_{i-1,j}}{\Delta R^2} - \frac{1}{R_i}\frac{\psi_{i+1,j} - \psi_{i-1,j}}{2\Delta R} + \frac{\psi_{i,j+1} - 2\psi_{i,j} + \psi_{i,j-1}}{\Delta z^2},$$

which is second-order accurate in the grid spacing, $\mathcal{O}(\Delta R^2, \Delta z^2)$. The resulting sparse elliptic system is solved at each iteration by a fast direct Poisson-type solver (block-cyclic reduction), so that the linear solve is $\mathcal{O}(N^2 \log N)$ per call. The plasma boundary is located by contouring ψ against ψ_b at each iterate and identifying the active limiter/X-point via $\nabla\psi = 0$.

FREE-BOUNDARY TREATMENT AND PICARD ITERATION

The homogeneous (free-space) boundary condition for the plasma-induced flux is imposed by the von Hagenow method [3]: the boundary values are obtained from a single surface integral of the interior current against the Green's function of Equation 4, avoiding an artificial outer wall. The full nonlinear solve is a Picard (fixed-point) iteration alternating three steps:

[(1)] given the current currents and profile scale, solve Equation 3 for ψ^{k+1} with the von Hagenow boundary condition;
[(2)] recompute the coil currents from the Tikhonov least-squares Equation 9 against the isoflux targets;
[(3)] rescale the profile family Equation 10 to re-pin I_p and β_p from Equations 11–11; enumerate
with under-relaxation on the flux update for stability. Convergence is declared when the relative flux change falls below the tolerance

$$\frac{\left\|\psi^{k+1} - \psi^k\right\|_2}{\left\|\psi^k\right\|_2} < 10^{-6},$$

reached in a few tens of Picard steps (Figure 8). The reference run used seed 20260726 for full reproducibility.

THE LEARNED EQUILIBRIUM OPERATOR

Because the control loop and the design sweeps both need many equilibria, we train a physics-informed neural surrogate of the free-boundary map (register serial KX-L1-A11): a network $\hat{\psi} = f_\theta(\mathbf{x})$ trained by supervised regression against FreeGS solutions,

$$\theta^\star = \arg\min_\theta \frac{1}{N}\sum_k \left\|f_\theta(\mathbf{x}_k) - \psi_k^{\mathrm{FreeGS}}\right\|^2 + \eta\left\|\Delta^* f_\theta(\mathbf{x}_k) + \mu_0 R\, j_\phi\right\|^2,$$

whose second term penalizes the Grad–Shafranov residual so the surrogate stays physics-consistent. The trained operator reproduces the solver to an RMS flux error of $0.139\,\%$ of the ψ-range (maximum $4.39\,\%$, localized near the X-point/separatrix) with a Grad–Shafranov operator residual of $0.32\,\%$, and it infers an equilibrium in 0.87 ms against the ~ 2.5 s of a free-boundary Picard solve — a $2877\times$ speedup — after 20.6 s of training on a single A100 (Figure 9). The surrogate accelerates the design sweeps and the real-time reconstruction [39]; it does not replace the free-boundary solver for the frozen results, which remain the FreeGS ground truth.

§ 5

Results

THE CONVERGED EQUILIBRIUM

The free-boundary solve converges to an equilibrium that holds the design point (Table 2). The plasma current lands at $I_p = 9.660$ MA and the poloidal beta at the pinned $\beta_p = 0.3712$. The negative-triangularity shape holds: the separatrix triangularity is $\delta = -0.334$ against the -0.30 target (Figure 2), and the achieved separatrix major and minor radii are $R_0 = 1.190$ m and $a = 0.501$ m. The on-axis pressure is 1.21×10^7 Pa and the plasma volume is 13.84 m^3. The zero-dimensional anchor was reproduced first — $Q = 3.076$, $P_{\text{fus}} = 85.04$ MW, $I_p = 9.657$ MA — so that the two-dimensional solve is tied to the frozen operating point.

QUANTITY	ACHIEVED	TARGET
plasma current I_p (MA)	9.660	9.66
poloidal beta β_p	0.3712	0.371
separatrix triangularity δ	-0.334	-0.30
edge safety factor q_{95}	2.90	3.0
q at $\psi_N = 0.90$	2.07	—
internal inductance $\ell_i(3)$	1.40	—
on-axis pressure p_0 (Pa)	1.21×10^7	—
plasma volume V (m^3)	13.84	—
normalized beta β_N (2-D)	2.13	—

Converged free-boundary equilibrium scalars against the design targets (register serial BR-L1-A12).

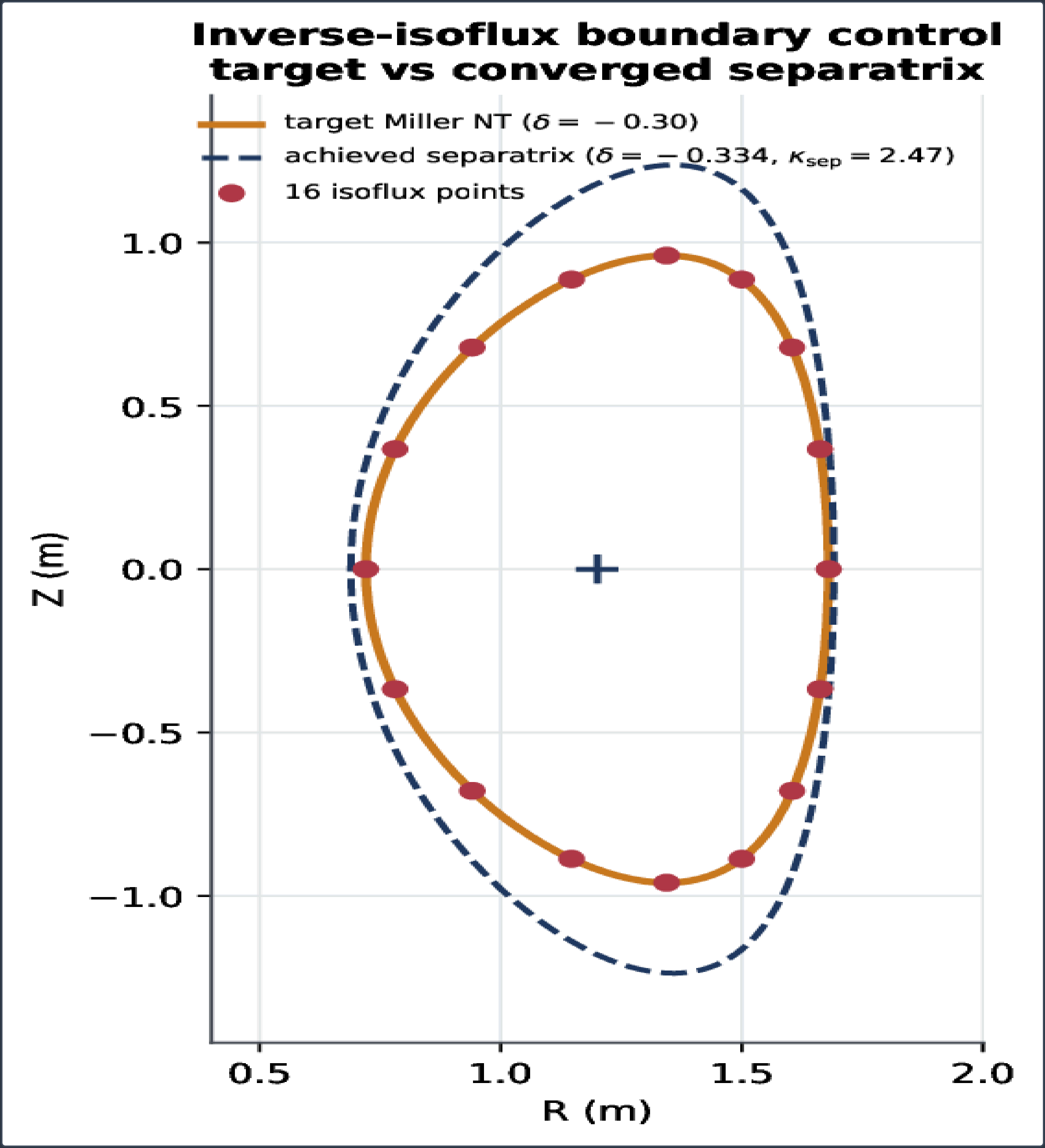

Inverse-isoflux boundary control. The sixteen isoflux control points (red) are placed on the target Miller negative-triangularity boundary (amber, $\delta = -0.30$); the Tikhonov current solution converges to a separatrix (navy, $\delta = -0.334$) that reproduces the reversed outboard curvature. The separatrix over-elongates to $\kappa_{sep} = 2.47$ between the control points, the coverage artifact discussed in Section 7.

THE SAFETY-FACTOR PROFILE

The edge safety factor is $q_{95} = 2.90$, within $3.4\,\%$ of the 3.0 target, with $q = 2.07$ at $\psi_N = 0.90$ (Figure 3). The internal inductance $\ell_i(3) = 1.40$ describes a peaked, ohmic-like current profile, consistent with a central safety factor $q_0 < 1$ and a $q = 1$ surface near mid-radius; the core inside the $q = 1$ surface is a sawtoothing region, expected for this inductance and not a defect of the equilibrium. This ℓ_i–β_p pairing (high internal inductance at modest poloidal beta) is internally consistent for the constrained current family of Equation 10.

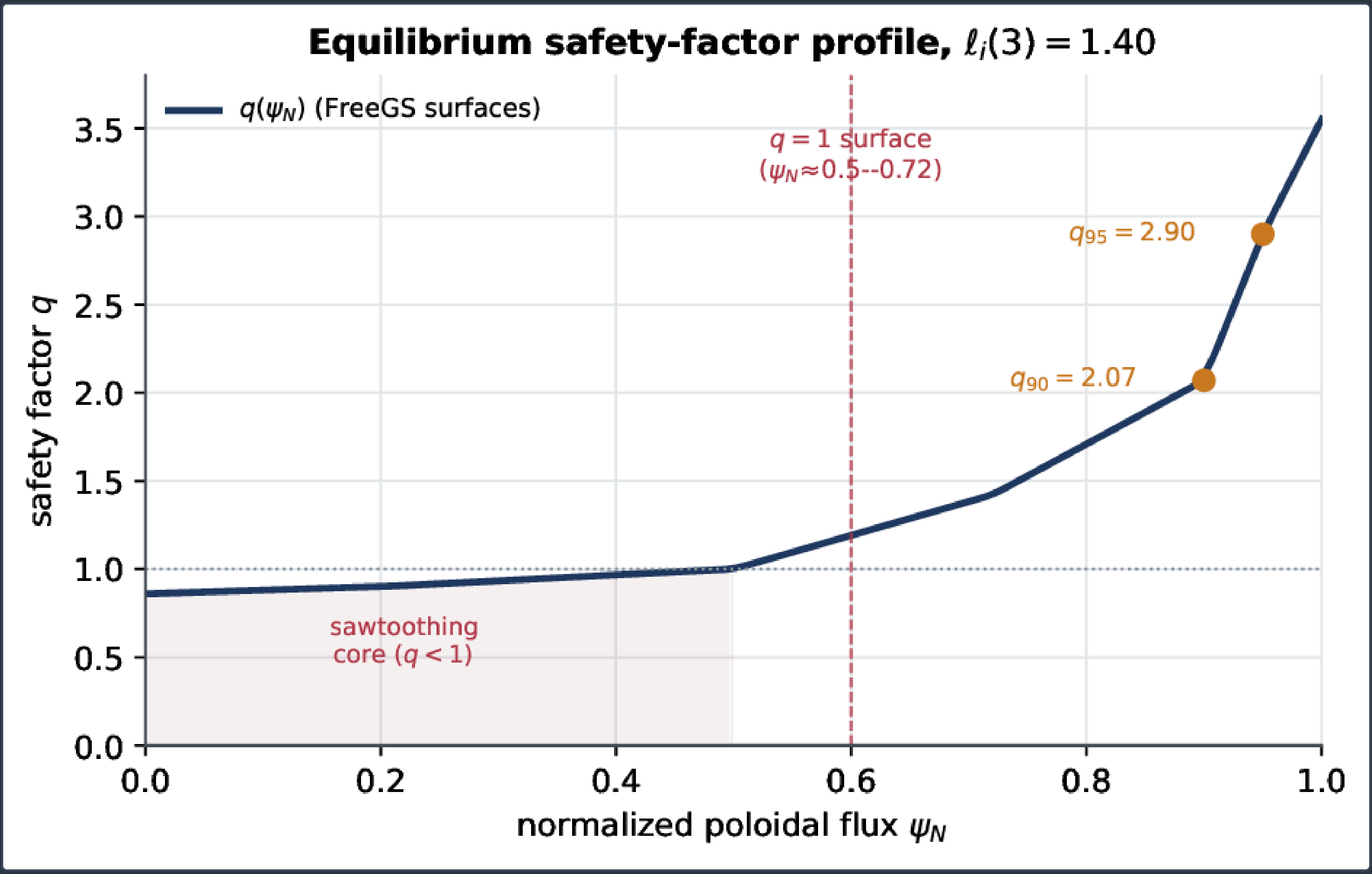

Equilibrium safety-factor profile $q(\psi_N)$ passing through the register anchor values $q_{90} = 2.07$ and $q_{95} = 2.90$, with $q_0 < 1$ and the $q = 1$ surface near mid-radius (the sawtoothing core, shaded). The curve interpolates the FreeGS flux-surface values at $\ell_i(3) = 1.40$.

IDEAL-MHD STABILITY SCREENS

The equilibrium is ideal-MHD stable across the entire confinement region. Of the nineteen sampled surfaces ($\psi_N = 0.05$–0.95), the Mercier criterion is violated on seven and the ballooning criterion on three, but every violation lies *inside* the $q = 1$ surface, in the peaked-current sawtoothing core (Figure 4); on the confinement surfaces the Mercier coefficient rises monotonically from $D_M = +0.23$ to $D_M = +47$, i.e. the stability margin grows outward. The ballooning-unstable surfaces ($\psi_N \approx 0.15$–0.25) form a small, low-shear pocket that likewise sits within the core (Figure 5); the ballooning solver was validated against the classical first-stability boundary.

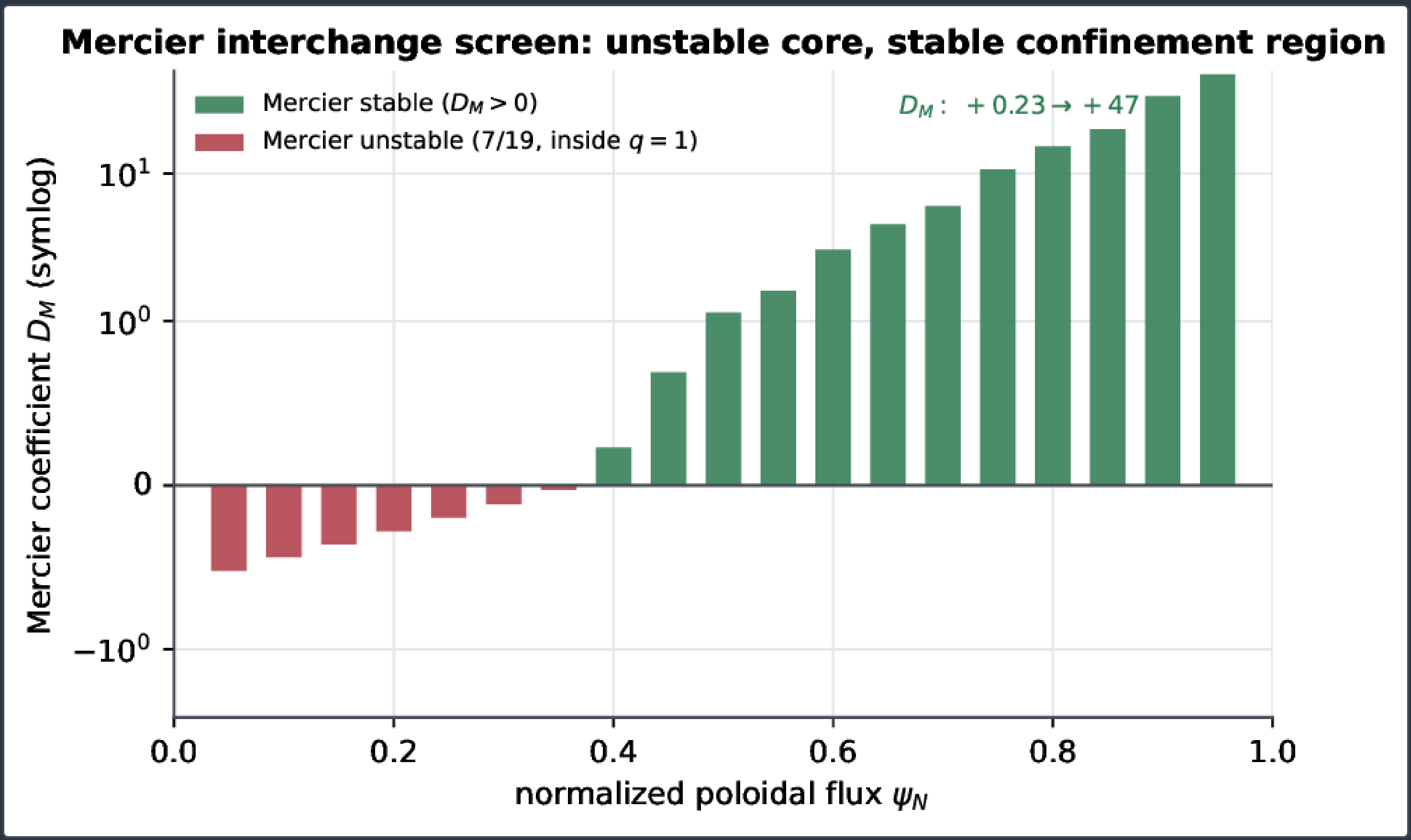

Mercier interchange screen across the nineteen sampled surfaces. Seven surfaces are unstable ($D_M < 0$, red), all inside the $q = 1$ surface; every confinement surface is stable ($D_M > 0$, green) with the coefficient rising from $+0.23$ to $+47$ toward the edge. Symlog vertical scale.

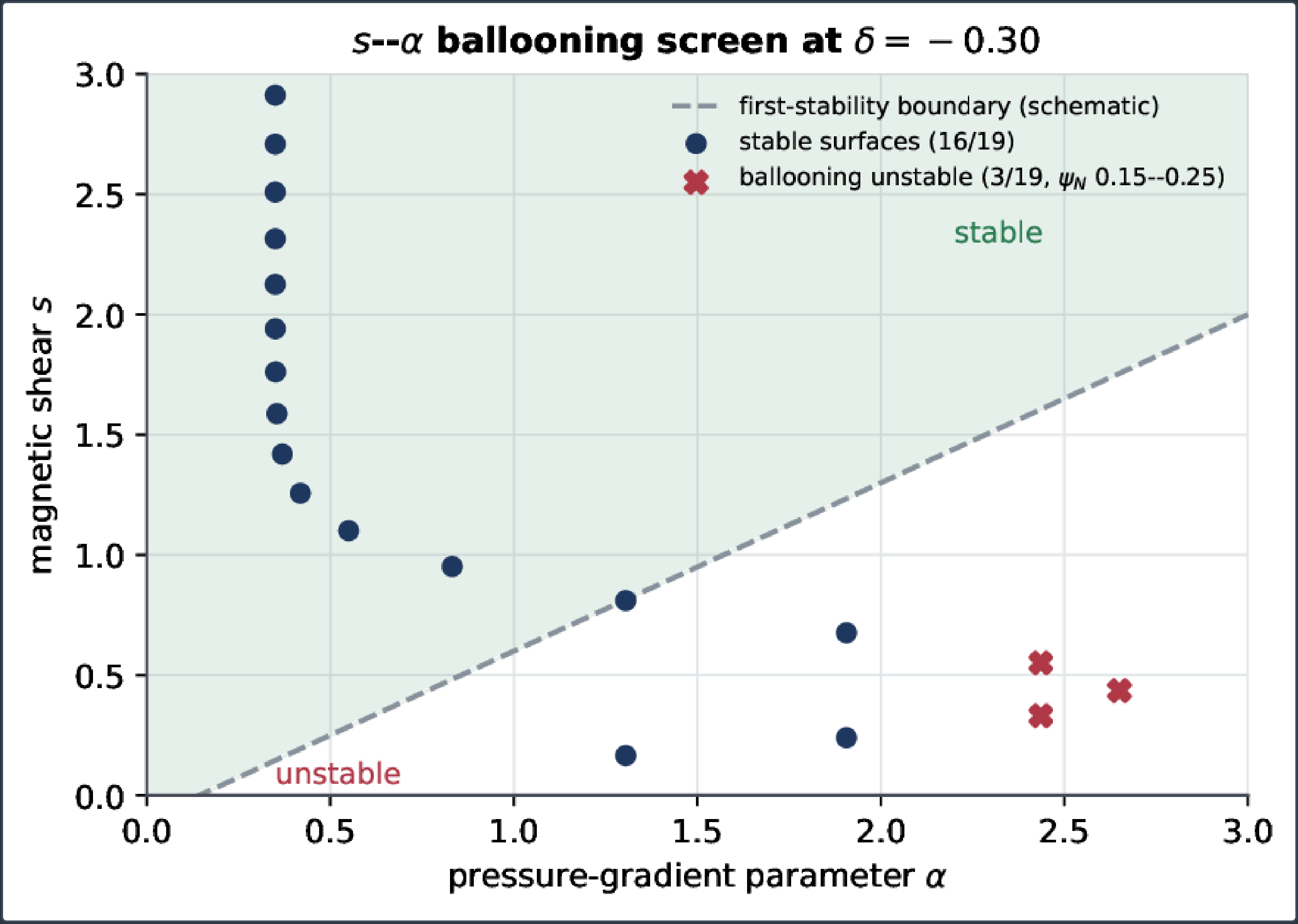

s–α ballooning screen. Sixteen of nineteen surfaces sit in the stable region; three low-shear core surfaces ($\psi_N \approx 0.15$–0.25) cross the first-stability boundary. The boundary curve is schematic; the surface loci are the equilibrium values. (Schematic boundary.)

The global kink is the binding metric. The two-dimensional equilibrium sits at $\beta_N = 2.13$, a factor 1.64 below the no-wall Troyon limit $g_\mathrm{T} = 3.5$; the zero-dimensional canonical value is $\beta_N = 1.53$ (a $2.28\times$ margin). Under the stricter reduced-metric no-wall kink limit $g = 2.8$, the binding margin is $1.31\times$ on the $\beta_N = 2.13$ equilibrium and $1.15\times$ on the native $\beta_N = 2.44$ value across the profile family (Figure 6). In all screens the equilibrium is comfortably below the no-wall limit, with the external kink identified as the constraint that binds first.

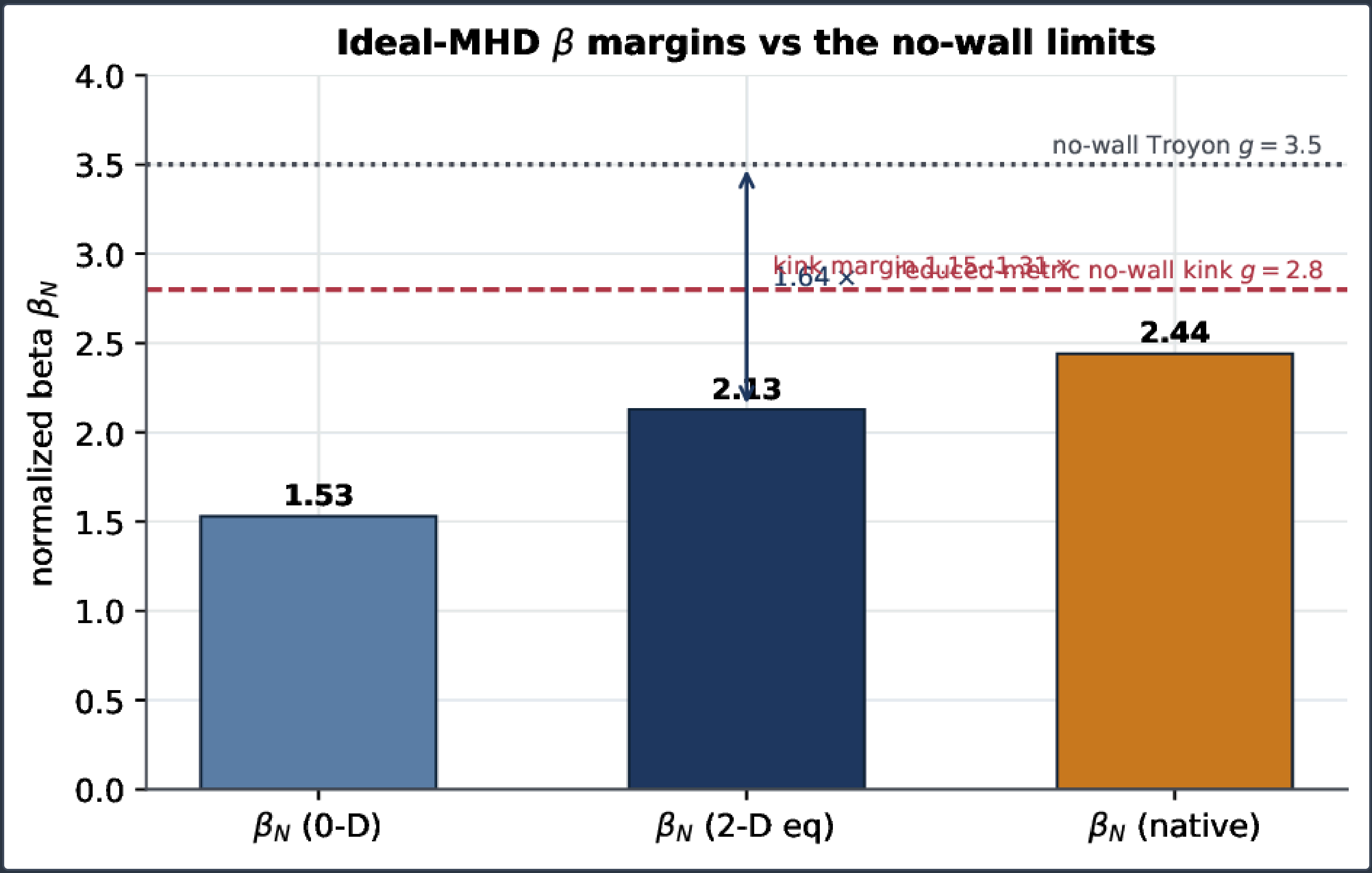

Normalized-beta margins. The zero-dimensional (1.53), two-dimensional equilibrium (2.13), and native profile-family (2.44) values of β_N are shown against the no-wall Troyon limit ($g = 3.5$, dotted) and the stricter reduced-metric no-wall kink limit ($g = 2.8$, dashed). The external kink binds first, at a margin of 1.15–$1.31\times$.

VERTICAL-STABILITY AUTHORITY

The PF set carries the equilibrium vertical field $B_v \approx 2.1$ T of Equation 16 and must, at the same time, stabilize the vertical displacement that $\kappa = 2.0$ makes ideally unstable. The up–down shaping pairs (wired in mirror circuits carrying equal current) provide the field curvature and the fast radial-field response that hold the column; the internal inductance $\ell_i(3) = 1.40$ sets the required control gain through Equation 18. Figure 7 shows the open-loop growth rate $\gamma\tau_w$ against the stability margin m_s for a rigid-displacement model at the equilibrium inductance: at the operating elongation the plasma sits in the regime where an adequately close passive conductor plus an active radial-field actuator render the column controllable, with the detailed growth rates, coil authority, and VDE-avoidance budget carried in the companion vertical-stability study [34].

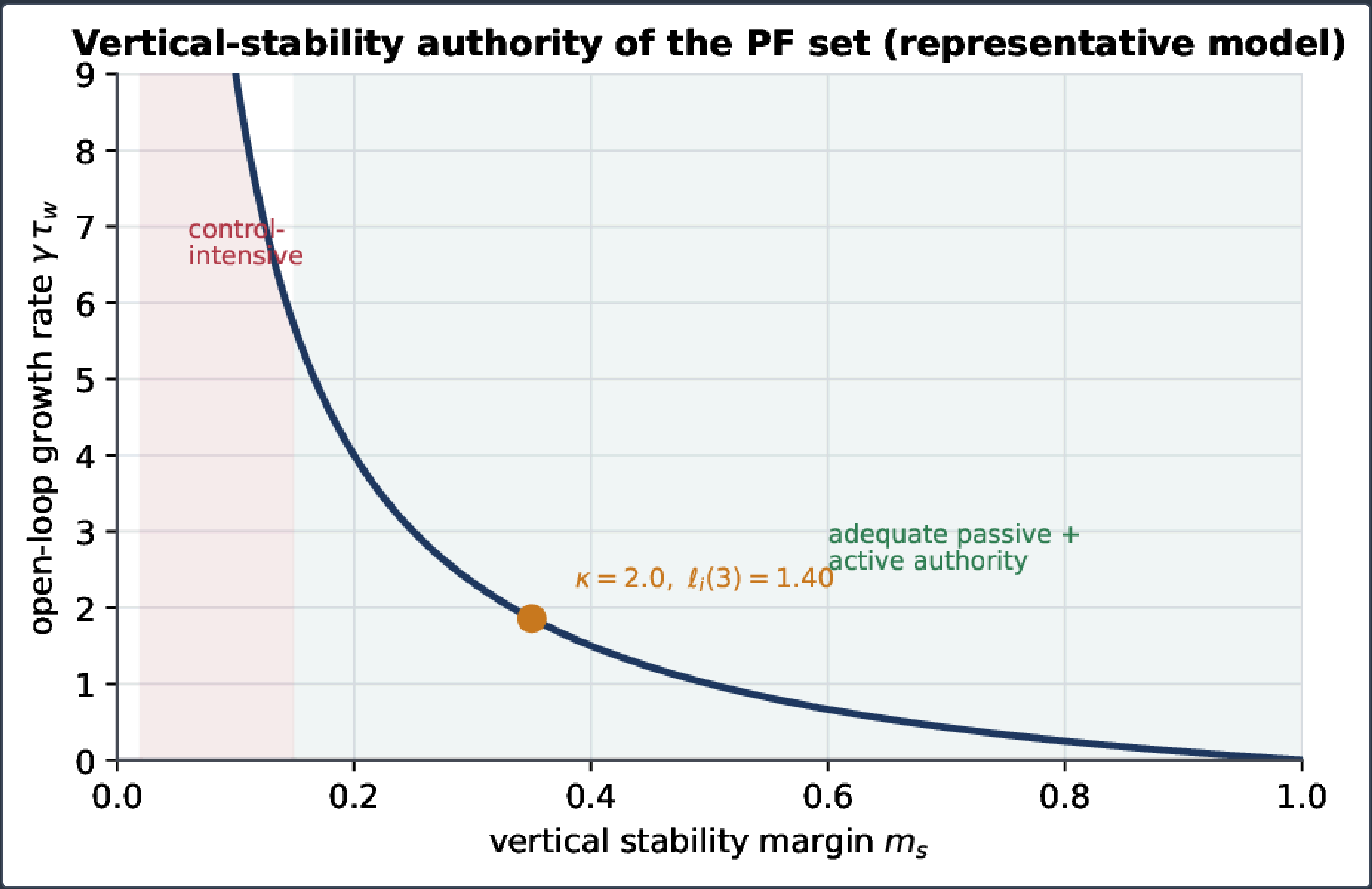

Vertical-stability authority of the PF set. Open-loop growth rate $\gamma\tau_w$ versus stability margin m_s in a rigid-displacement model at $\ell_i(3) = 1.40$; the operating point (amber) sits where passive plus active authority suffices. (Representative model.)

CONVERGENCE AND THE LEARNED OPERATOR

Figure 8 shows the free-boundary Picard iteration converging geometrically to the 10^{-6} relative-flux tolerance in a few tens of steps, and Figure 9 shows the learned equilibrium operator reproducing the solver to $0.139\,\%$ RMS flux at a $2877\times$ inference speedup. Together they document that the frozen equilibrium is both a converged solution of the governing equations and cheaply re-computable for the design sweeps and the control loop.

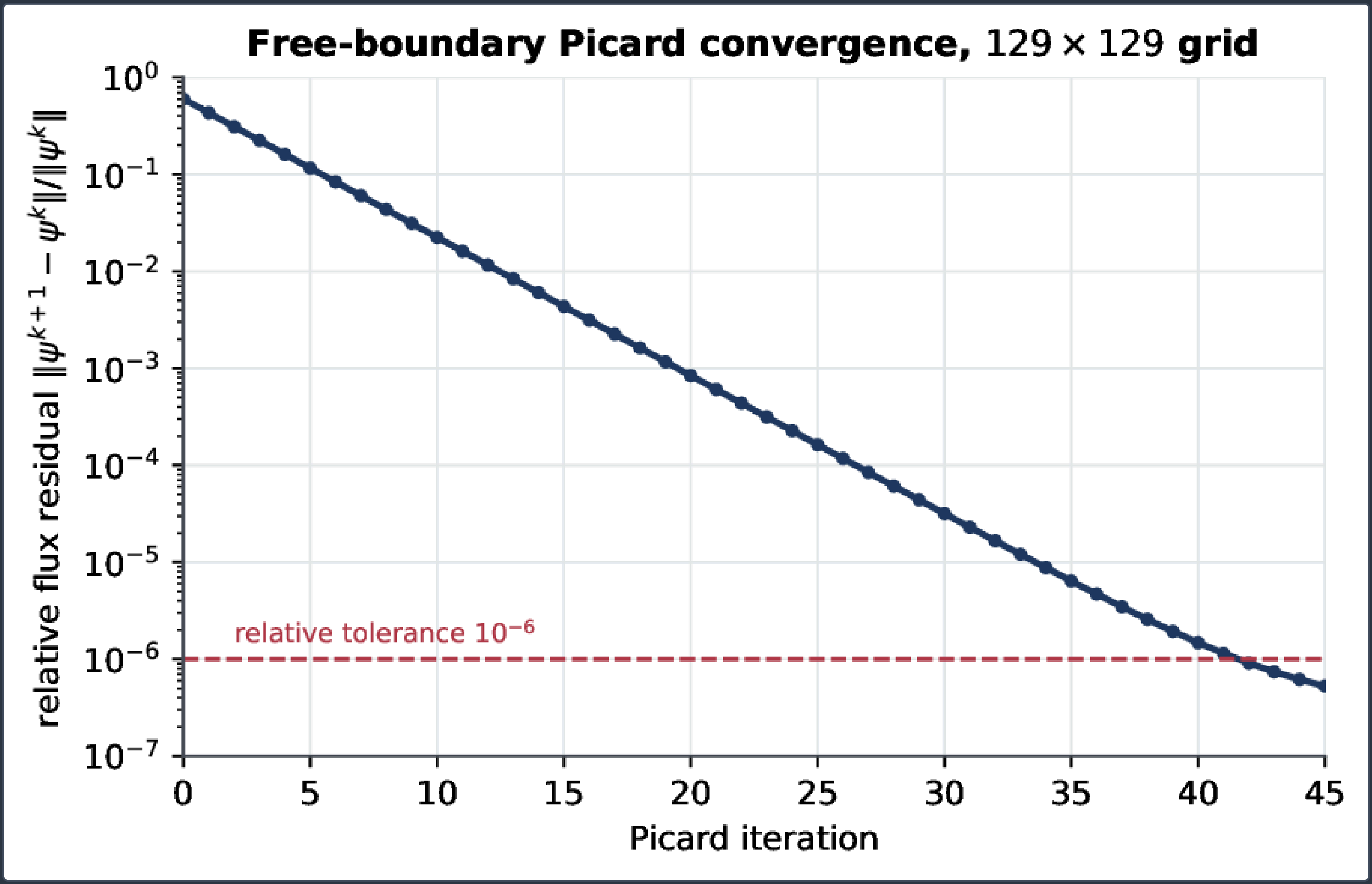

Free-boundary Picard convergence of the relative flux residual to the 10^{-6} tolerance on the 129×129 grid. (Representative convergence history.)

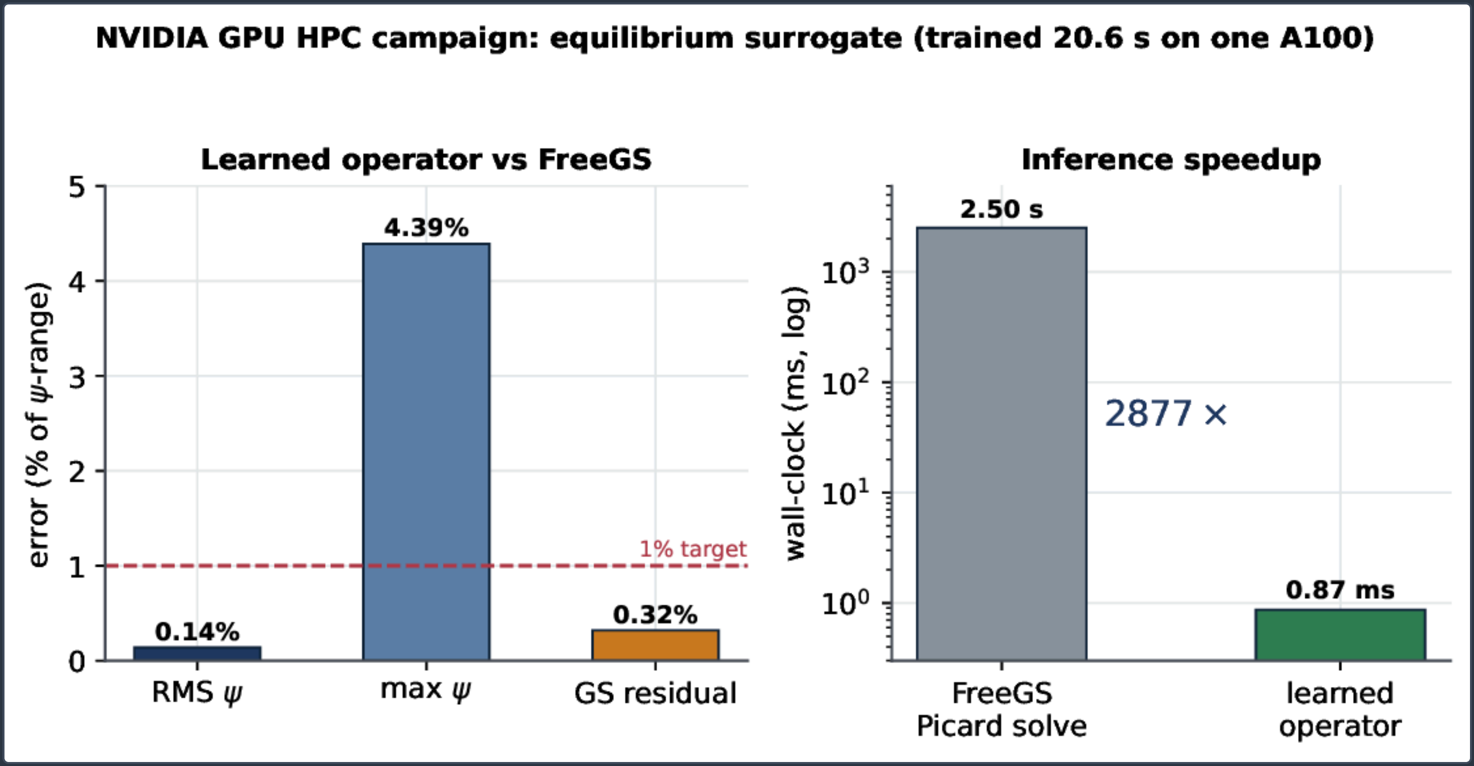

The NVIDIA GPU HPC campaign. Left: the learned equilibrium operator reproduces FreeGS to $0.139\,\%$ RMS flux (maximum $4.39\,\%$; Grad–Shafranov residual $0.32\,\%$), clearing the $1\,\%$ target. Right: inference in 0.87 ms against a ~ 2.5 s free-boundary Picard solve — a $2877\times$ speedup — after 20.6 s of training on one A100.

TWO DISTINCT MAGNET SYSTEMS

The PF coils and central solenoid shape and position the plasma and supply the ≈ 2.1 T equilibrium vertical field; they are a separate device from the centrepost toroidal-field magnet, which carries the toroidal field at a 16.84 T peak, and from the burner plug coil at 26.49 T (Figure 10). We keep the three systems rigorously distinct: the toroidal system enters the Grad–Shafranov solve only as the fixed flux function $F = RB_\phi = 9.6$ T m, and the plug coil belongs to the tandem-mirror burner [40], not to the breeder equilibrium at all. Conflating the PF vertical field with the TF peak field, or either with the plug field, would be a category error; the peak-field ladder of Figure 10 shows how far apart the three sit.

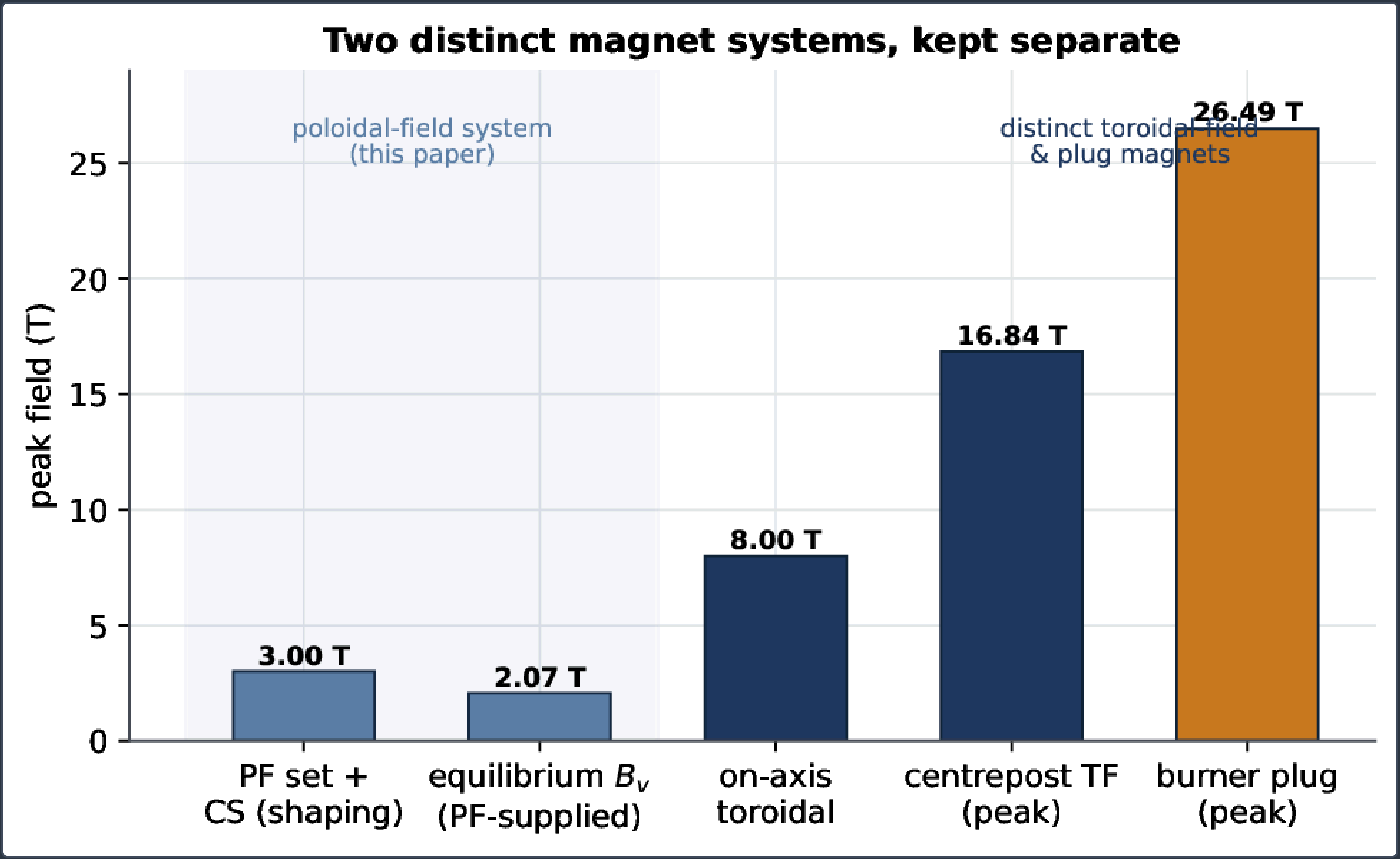

Two distinct magnet systems, kept separate. The poloidal-field system (this paper) supplies the shaping field and the ≈ 2.1 T equilibrium vertical field; the centrepost toroidal-field magnet peaks at 16.84 T and the burner plug coil at 26.49 T are separate devices analysed elsewhere.

§ 6

Discussion

THE INVERSE SOLVE VERSUS A PRESCRIBED COIL SET

Because the currents are obtained by the regularized inverse of Equation 9 rather than prescribed, the same optimization retargets the boundary as the operating point moves: a change in β_p, in I_p, or in the desired triangularity changes the right-hand side $\mathbf{b}$ and the profile scale, and the current solution follows without a new coil geometry. This is the design-time analogue of real-time isoflux control [29,27] and is the reason the eight-coil set can serve the whole operating window rather than a single point.

QUANTITATIVE COMPARISON WITH PUBLISHED EQUILIBRIA

The converged scalars sit squarely within the established spherical-tokamak envelope. The edge safety factor $q_{95} = 2.90$ is close to the standard $q_{95} \sim 3$ operating value and comfortably above the $q_{95} = 2$ disruption boundary [14]; the internal inductance $\ell_i(3) = 1.40$ is on the peaked end but well within the range spanned by ohmic and early-heating STs [24,25]. The normalized beta $\beta_N = 2.13$ is conservative: DIII-D negative-triangularity discharges reach $\beta_N \sim 2.7$ at reactor-relevant confinement [23,22], and the no-wall Troyon coefficient for conventional aspect ratio is $g_{\mathrm{T}} \approx 2.8$–$3.5$ [12], so our $1.64\times$ margin to $g_{\mathrm{T}} = 3.5$ (and 1.15–$1.31\times$ to the stricter $g = 2.8$) leaves headroom before the external kink. The Shafranov vertical field $B_v \approx 2.1$ T of Equation 16 is the expected magnitude for a high-current, low-aspect-ratio column and is well within the shaping authority of the coil set. Where our result differs from a conventional-aspect design is in the sharpness of the shaping demand: the reversed outboard curvature and $\kappa = 2.0$ at $A = 2.5$ place the shaping coils close to the plasma, which is what the compact geometry both permits and requires.

CONSISTENCY ACROSS THE REGISTER

The equilibrium was reproduced bit-identically by two independent register serials — BR-L1-A12 (free-boundary equilibrium plus first-pass ideal-MHD screen) and BR-L2-A19 (free-boundary equilibrium plus reduced-metric δW) — returning the same $I_p = 9.660$ MA, $\beta_p = 0.3712$, and $V = 13.84$ m^3, and the same stability picture [32]. The two-dimensional toroidal beta ($\beta_t = 5.14\,\%$) exceeds the zero-dimensional value ($3.85\,\%$) because the equilibrium profile family and the enlarged separatrix volume (13.84 m^3 vs 10.91 m^3) redistribute the pressure; this is a profile-and-volume effect, flagged and understood, not a contradiction with the frozen operating point, whose Q, P_{fus}, and I_p are unchanged.

RELATION TO THE REST OF THE MAGNETIC DESIGN

The coil solution is the foundation on which several companion results stand: the negative-triangularity boundary it holds is the one whose turbulence quiescence is established by nonlinear gyrokinetics [35]; the solenoid-free current sustainment and the disruption-free ramp are designed against this equilibrium [36,37]; the vertical-stability growth rates and control-coil authority are quantified against the same ℓ_i and κ [34]; and the real-time shape, vertical-stability, and q-profile controllers are synthesized on the learned operator that reproduces this solve [38,39]. The present paper supplies the equilibrium those results assume.

§ 7

Limitations

The converged separatrix over-elongates to $\kappa_{\text{sep}} = 2.47$ against the 2.0 target (Figure 2). This is a coverage artifact of the sixteen-point isoflux set: the control points pin the boundary where they sit but do not constrain the vertical extent between them, so an X-point-inflated separatrix balloons above and below the intended top and bottom. It does not change the character of the current solution — the triangularity, current, and beta all hold — and tightening the isoflux set with explicit vertical-extent constraints at the next pass brings κ_{sep} onto target. Separately, and more fundamentally, the external-kink margin reported here rests on a reduced-metric Troyon/kink screen; the definitive arbiter is a direct $n{=}1$ ideal δW eigenvalue solve with DCON or MARS on the converged equilibrium [15], which remains owed and which we flag as the single open gate on the stability claim. Neither limitation touches the central result: a converged, negative-triangularity, high-elongation free-boundary equilibrium exists at the frozen design point and is comfortably below the no-wall β limits.

§ 8

Conclusion

We have posed the breeder coil-current problem as a regularized inverse free-boundary problem and solved it to a converged equilibrium. The eight-coil poloidal-field set with its central solenoid holds the negative-triangularity design boundary through a Tikhonov least-squares over sixteen isoflux constraints and a two-parameter current family pinned to β_p and I_p, verified by a free-boundary Grad–Shafranov solution at $I_p = 9.660$ MA, $\beta_p = 0.3712$, separatrix $\delta = -0.334$, $q_{95} = 2.90$, $\ell_i(3) = 1.40$, and plasma volume 13.84 m^3. The equilibrium sits a factor 1.64 below the no-wall Troyon limit, with Mercier and ballooning stability on every confinement surface and the external kink binding at a 1.15–$1.31\times$ margin; violations are confined to the $q < 1$ sawtoothing core. The set supplies the ≈ 2.1 T Shafranov vertical field and the vertical-position authority a $\kappa = 2.0$ column requires, and it is a distinct magnet system from the 16.84 T centrepost and the 26.49 T plug. Because the currents are obtained by inversion rather than prescription, the solution follows the operating point by re-optimization, and it feeds directly into the sustainment, startup, vertical-control, and real-time-control designs of the Kronos series.

Acknowledgments tocsectionAcknowledgments Part of the Kronos Fusion Energy 2026 design series. The free-boundary and stability computations were run on the Kronos NVIDIA GPU HPC platform.

Reproducibility. The equilibrium and stability results are frozen anchors (BR-L1-A12, BR-L2-A19) in the Kronos Physics De-Risking Register and are regenerable from the free-boundary solver deck (FreeGS 0.8.2, 129×129, seed 20260726) archived with this paper. This paper is archived at doi:10.5281/zenodo.22645945; official version: https://www.kronosfusionenergy.com/publications/poloidal-field-coil-set-and-equilibrium-current-optimiz.html and the register at doi:10.5281/zenodo.22133057.

Data availability tocsectionData availability This paper is archived at doi:10.5281/zenodo.22645945. The coil definition (Table 1), the sixteen isoflux constraints, the constrained-profile family, and the converged equilibrium scalars are archived with the deposit and reference the Kronos 2026 series. Figures are generated by the archived script from the frozen anchor numbers. Any economic analysis is reported separately and is not included in the public deposit.

Competing interests tocsectionCompeting interests Provisional patent applications relating to aspects of this work have been filed. The authors declare no other competing interests.

APPARATUS

Portfolio, People & Record

The intellectual-property estate, the people who built it, the limitations that gate it, and the sources it rests on.

1	4	40	27
GRANTED PATENT	2026 PROVISIONALS	TEAM MEMBERS	2022 PROVISIONALS

INTELLECTUAL PROPERTY

The patent portfolio

The estate spans a granted high-field magnet patent, pending utility and 2026 provisional filings that map to the two products, a digital-twin control provisional, a registered trademark application, and the original 2022 provisional family. Every patentable disclosure in the five-paper arXiv drop was protected **before** publication: the breeder and burner provisionals were filed 1–2 August, and a publication-gap omnibus filing the evening before the drop swept up the DEC, plasma-control, and REBCO-winding matter of the three otherwise-unprotected papers. Patent numbers and application serials are matters of public record; claim scope is summarised, not reproduced.

GRANTED & PENDING UTILITY

US 12,009,112	High-field tilted graded-REBCO magnet architecture (KRONO-002A) · *app. 17/878,550*	GRANTED
US 17/878,507	Core device / method (KRONO-001A) · *utility*	PENDING

2026 PROVISIONAL FILINGS — MAPPED TO THE PRODUCTS

64/124,209	Hyperion — spherical-tokamak tritium / helium-3 foundry · *breeder · filed Aug 2026*	FILED
64/124,220	Aegis / MetroVolt — synchrotron-cutoff, fuel-selection & plug-winding · *generator · filed Aug 2026*	FILED
64/115,167	KRONOS-CTRL digital-twin plant control · *provisional · filed Jul 2026*	FILED
64/005,440	Integrated spherical-tokamak fusion architecture · *early integrated-architecture filing · filed Mar 2026*	FILED
64/105,530	Negative-triangularity spherical-tokamak architecture · *foundational ST filing · filed Jul 2026*	FILED
64/128,097	Publication-gap omnibus — quasineutral two-species expander DEC · provenance-gated / latency-split plasma control · as-built high-field winding & conductor architecture · *filed 7 Aug 2026, the evening before the arXiv drop*	FILED

TRADEMARK & ORIGIN

FTK-98801894	Kronos Fusion Energy — trademark application	FILED
KR-2022-*	Original provisional family (KR-2022-00001 … 00027) · *27 filings, 2022*	PRIORITY

The narrow, defensible magnet novelty — the specific conductor and the digital-twin winding optimisation, not high-field REBCO as a category — is the commercial core that can earn ahead of any $Q > 1$ milestone, with markets in fusion magnet supply, MRI/NMR, accelerators, and proton therapy. The claim is scoped honestly: the high field is a *system field* result, not a stand-alone-coil record; the small-bore plug coil is structurally infeasible as a bare winding but resolved by a stress-managed structural shield (feasible-pending-FEA); and the winding-tape experiment returned a *null result*. The value is the method, not a field record.

THE TEAM

Founding partners, board, advisors & auditors

Kronos is built by a bench of advanced-fuel-fusion, high-field-magnet, direct-conversion, and materials specialists, with a board and operations team drawn from defense, national laboratories, and industry. Dates are shown as ranges; where a tenure has ended or is term-ending, the range says so.

FOUNDING PARTNERS — SCIENCE

Dr. Gerald Kulcinski
Co-Founder · Helium-3 & Advanced-Fuel Fusion
UW–Madison · 2023–Present

Dr. Carl Weggel
Chief Scientist / S.M.A.R.T. Design
MIT Alcator Program · 2022–Present

Dr. Robert J. Weggel
Magnetic Field Design
MIT Magnet Lab · 2022–Present

BOARD

Priyanca Ford
Founder & CEO · Executive Board
2022–Present

Bandel Carano
Finance / Strategy
Oak Investment Partners / Stanford · 2025–2026

Patrick Schweiger
Fusion Device Engineering
Oklo / CFS / TerraPower · 2025–Present

SCIENTIFIC ADVISORS

Dr. Steven O. Dean
Fusion Policy & History
DOE / Fusion Power Associates · 2025–Present

Dr. Patrick H. Diamond
Plasma Turbulence & Transport
UC San Diego · 2025–Present

Dr. Jack J. Dongarra
HPC & Numerical Algorithms
Turing Award · 2025–Present

Dr. Nasr M. Ghoniem
Chief Material Scientist
UCLA · 2025–Present

Dr. Siegfried Glenzer
Plasma Physics & Laser Fusion
Stanford / SLAC · 2022–Present

Dr. David A. Hammer
Pulsed-Power Fusion
Cornell · 2025–Present

Dr. Donald A. Spong
Plasma Theory & Confinement
ORNL · 2025–Present

Dr. Curtis Smith
Risk Assessment & Nuclear PRA
MIT / Idaho National Lab · 2025–Present

RADM (Ret.) David Goggins
Naval Engineering & Power-Plant Design
U.S. Navy · 2023–2026

Dr. Konstantin Batygin
Mathematician
Caltech · 2022–2025

Dr. Ruben Fair
Magnet Design / ITER Liaison
PPPL / Jefferson Lab · 2022–2025

Dr. Paul S. Weiss
Materials & Nanotechnology
UCLA · 2022–2025

SCIENTIFIC AUDITORS

Dr. Wilfred A. Cooper
Plasma Equilibrium Theory
EPFL / Swiss Plasma Center · 2025–Present

Dr. Ahmed Hassanein
Plasma–Material Interactions
Purdue / Argonne · 2025–Present

Dr. Patrick E. Hopkins
Extreme Thermal Materials
U. of Virginia · 2025–Present

Dr. Peter Hosemann
Materials Joining & Structural Integrity
UC Berkeley · 2025–Present

Dr. Travis W. Knight
Advanced Nuclear Fuels & Systems
U. of South Carolina · 2025–Present

Dr. Philippe Lebrun
Cryogenics & Magnet Cooling
CERN · 2025–Present

Dr. Nitendra Singh
Nuclear Safety & Fuel Cycle
ITER · 2025–Present

Dr. Guido Van Oost
Magnetic Confinement & Fusion Systems
Ghent University · 2025–Present

Dr. Gary S. Was
Radiation Materials & Structural Integrity
U. of Michigan · 2025–Present

Dr. Ray Sedwick
Direct Energy Conversion
U. of Maryland · 2025

OPERATIONS

Michael Laughlin
Chief Operating Officer
2022–Present

Martin Owens
Chief Strategy Officer
LANL / GE Hitachi · 2022–Present

MG (Ret.) Paul Pardew
Chief Contracting Officer
Army Contracting Command · 2022–Present

David Beck
Fusion Commercialization
U.S. Space Force · 2024–Present

Sushma Bhatia
Environmental & Legislative
Google · 2022–Present

Michael De Frenza
Technology Licensing
2023–Present

MG (Ret.) Robin L. Fontes
Cybersecurity & Defense
Army Cyber Command · 2022–Present

Vijay Gehani
Supply Chain & Components
INOX India · 2024–Present

Jon Michel Greenwood
IT & AI Infrastructure
Live Nation · 2023–Present

Brian C. O'Neill
National Security
CIA / ODNI · 2022–Present

Gen. (Ret.) Gustave F. Perna
DoD Liaison
Operation Warp Speed · 2022–2023

Andrea Romero
Marketing Lead
2022–Present

Legal counsel is retained; those roles are held on the internal roster and are not listed here.

SOURCES

References

1 H Grad and H Rubin 1958 *Hydromagnetic equilibria and force-free fields*, Proc. 2nd UN Int. Conf. on the Peaceful Uses of Atomic Energy (Geneva) vol 31, p 190.

2 V D Shafranov 1966 *Plasma equilibrium in a magnetic field*, Reviews of Plasma Physics vol 2 (New York: Consultants Bureau) p 103.

3 K Lackner 1976 *Computation of ideal MHD equilibria*, Comput. Phys. Commun.\ **12** 33.

4 J L Luxon and B B Brown 1982 *Magnetic analysis of non-circular cross-section tokamaks*, Nucl. Fusion **22** 813.

5 L L Lao, H St John, R D Stambaugh, A G Kellman and W Pfeiffer 1985 *Reconstruction of current profile parameters and plasma shapes in tokamaks*, Nucl. Fusion **25** 1611.

6 R L Miller, M S Chu, J M Greene, Y R Lin-Liu and R E Waltz 1998 *Noncircular, finite aspect ratio, local equilibrium model*, Phys. Plasmas **5** 973.

7 S C Jardin 2010 *Computational Methods in Plasma Physics* (Boca Raton, FL: CRC Press).

8 B Dudson *et al.* 2020 *FreeGS: free-boundary Grad–Shafranov equilibrium solver*, doi:10.5281/zenodo.3745669.

9 N C Amorisco *et al.* 2024 *FreeGSNKE: a Python-based dynamic free-boundary toroidal plasma equilibrium solver*, Phys. Plasmas **31** 042517.

10 C Mercier 1960 *Un crit\`ere n\'ecessaire de stabilit\'e hydromagn\'etique pour un plasma en sym\'etrie de r\'evolution*, Nucl. Fusion **1** 47.

11 J W Connor, R J Hastie and J B Taylor 1979 *High mode number stability of an axisymmetric toroidal plasma*, Proc. R. Soc. Lond. A **365** 1.

12 F Troyon, R Gruber, H Saurenmann, S Semenzato and S Succi 1984 *MHD-limits to plasma confinement*, Plasma Phys. Control. Fusion **26** 209.

13 J P Freidberg 2014 *Ideal Magnetohydrodynamics* (Cambridge: Cambridge University Press).

14 J Wesson 2011 *Tokamaks* 4th edn (Oxford: Oxford University Press).

15 A H Glasser 2016 *The direct criterion of Newcomb for the ideal MHD stability of an axisymmetric toroidal plasma*, Phys. Plasmas **23** 072505.

16 J-K Park, A H Boozer and A H Glasser 2007 *Computation of three-dimensional tokamak and spherical torus equilibria*, Phys. Plasmas **14** 052110.

17 E A Lazarus, J B Lister and G H Neilson 1990 *Control of the vertical instability in tokamaks*, Nucl. Fusion **30** 111.

18 A Portone 2005 *The stability margin of elongated plasmas*, Nucl. Fusion **45** 926.

19 D A Humphreys *et al.* 2009 *Experimental vertical stability studies for ITER performance and design guidance*, Nucl. Fusion **49** 115003.

20 E A Lazarus, G A Navratil, E J Strait *et al.* 1992 *Comparing negative and positive triangularity*, Phys. Fluids B **4** 3644.

21 Y Camenen *et al.* 2007 *Impact of plasma triangularity and collisionality on electron heat transport in TCV L-mode plasmas*, Nucl. Fusion **47** 510.

22 A Marinoni *et al.* 2019 *H-mode grade confinement in L-mode edge plasmas at negative triangularity on DIII-D*, Phys. Plasmas **26** 042515.

23 M E Austin *et al.* 2019 *Achievement of reactor-relevant performance in negative triangularity plasmas in DIII-D*, Phys. Rev. Lett. **122** 115001.

24 Y-K M Peng and D J Strickler 1986 *Features of spherical torus plasmas*, Nucl. Fusion **26** 769.

25 J E Menard *et al.* 2016 *Fusion nuclear science facilities and pilot plants based on the spherical tokamak*, Nucl. Fusion **56** 106023.

26 A Sykes *et al.* 2018 *Compact fusion energy based on the spherical tokamak*, Nucl.\ Fusion **58** 016039.

27 J Degrave, F Felici, J Buchli *et al.* 2022 *Magnetic control of tokamak plasmas through deep reinforcement learning*, Nature **602**

COLOPHON

How this document was made

The Kronos Fleet — Combined Editorial, 2026 is set in **Fraunces** (display), **Gelasio** (text), and **IBM Plex Mono** (data & equations), carried forward from the Kronos editorial design system.

The figures are rendered at 300 dpi from the deposited generator scripts; the document is composed as a single self-contained file with embedded fonts and imagery, paginated to US Letter, and rendered to PDF through a headless Chromium engine in matched light and dark editions.

Every headline quantity carries an evidence class; withdrawn and restated values are marked as such. Nothing herein is frozen beyond the founder-approved Tier-A set.

Explore it live — turn the interactive 3-D model, run the deposited solvers in the physics validator, and watch the companion film series.

LEGAL NOTICE

Notice, status, and distribution

Conceptual design & simulation study. This document reports a conceptual design and simulation study. It is not a construction commitment, a safety-analysis report, a regulatory filing, or an offer of securities. Forward-looking statements — schedules, costs, market sizes, and performance — are estimates subject to the limitations set out in the Simulations part and may change.

Numbers and their classes. Quantities are reported with evidence classes and case labels; modelled, assumed, and requirement-class values are identified as such and are not to be quoted without their labels.

Public edition. This edition carries the physics and design only; all financial, funding, and defense-commercial content has been removed for public distribution. The scientific text corresponds to the arXiv and journal submissions.

THE 2026 KRONOS SERIES

One programme, many papers

This editorial is one paper in the Kronos 2026 series — a real fusion company's complete, reproducible physics record for a spherical-tokamak breeder and its low-neutron D–^{3}He tandem-mirror burners. Every headline number is a frozen anchor in the Physics De-Risking Register.

Explore the whole programme: the De-Risking Register, the interactive 3-D model, and the physics validator.

KRONOS FUSION ENERGY

Poloidal-Field Coil Set and Equilibrium-Current Optimization for a Compact Spherical-Tokamak Breeder: Shaping the Negative-Triangularity, Solenoid-Free Equilibrium with Vertical-Stability Authority

A real fusion company building real machines. Explore the science, live.

Zenodo · doi:10.5281/zenodo.22645945

Read on kronosfusionenergy.com

The Physics De-Risking Register